Numerical Investigation of Scale-2 and Scale-3 Haar Wavelet Approaches for Solving Elliptic Partial Differential Equations

Avinash K, Sharath Kumar Shettigar, and Harinakshi Karkera*

***Abstract*—This study presents a numerical investigation of Scale-2 and Scale-3 Haar wavelet methods for solving elliptic partial differential equations (PDEs) that describe steady-state heat distribution. The spatial derivatives are discretized using Scale-2 and Scale-3 Haar wavelet expansions, which are then integrated and extended to a 2D solution via Kronecker tensor product, incorporating boundary conditions through integration constants. The error analysis and convergence rate are performed to evaluate the numerical precision of the results. Computational simulations are carried out using MATLAB programming. Both the wavelet methods are compared with the existing finite difference method (FDM), and the results demonstrate that while all three approaches effectively solve elliptic PDEs, the Scale-3 Haar wavelet method outperforms the others by delivering more accurate approximate solutions with greater efficiency. The findings of this study highlight the potential and reliability of Haar wavelet methods for solving complex PDEs in various engineering applications.**

***Index Terms*—Convergence rate, error estimates, Haar wavelet, symmetric wavelet, antisymmetric wavelet, Kronecker product**

I. Introduction

PARTIAL differential equations (PDEs) are mathematical equations involving multiple independent variables, categorized into parabolic, hyperbolic, and elliptic equations based on the nature of their terms. They find extensive application in biological, chemical, and physical scenarios, capturing diverse interactions through mathematical models. Existing research studies have significantly focused on analyzing these models, enabling the development of reliable numerical solutions when precise parameter information and initial/boundary conditions are known. However, real-world complexities, with their inherent variability, pose challenges to accurate modeling. Despite these difficulties, the steady-state solutions of parabolic and hyperbolic equations often converge to solutions of second-order elliptic equations as time approaches infinity. For instance, modeling the steady-state heat distribution on a rectangular plate with specified edge temperatures exemplifies this behavior [1]–[3].

Manuscript received December 13, 2024; revised April 26, 2025.

Avinash K is a Research scholar in the Department of Mathematics, Manipal Institute of Technology, Manipal Academy of Higher Education, Manipal, Karnataka, 576104 India (e-mail: avinash.dscmpl2023@learner.manipal.edu).

Sharath Kumar Shettigar is a Research scholar in the Department of Mathematics, Manipal Institute of Technology, Manipal Academy of Higher Education, Manipal, Karnataka, 576104 India (e-mail: sharath.shettigar@learner.manipal.edu).

Harinakshi Karkera is an Assistant Professor in the Department of Mathematics, Manipal Institute of Technology, Manipal Academy of Higher Education, Manipal, Karnataka, 576104 India (*Corresponding author to provide phone: +91-9743287827; (e-mail: harinakshi.karkera@manipal.edu).

Because time is not a factor in this system, the heat distribution depends solely on the spatial coordinates x and y. This steady-state heat distribution equation has a wide variety of applications across various fields, including physics, chemistry, biology, and earth science, where understanding heat distribution is crucial. This article focuses on analyzing the linear, two-dimensional, steady-state heat distribution equation

$$\frac{\partial^2 u}{\partial x^2} + \frac{\partial^2 u}{\partial y^2} = g(x,y) \qquad (x,y) \in [A,B] \times [A,B] \quad (1)$$

where x and y are spatial coordinates that are independent, u is the dependent variable, and $g(x,y)$ is the heat source vector.

Numerical methods for solving PDEs, such as finite difference method [4], [5], finite element method [6], [7], spectral collocation method, and finite volume techniques [8], [9], finite line method [10], etc., have seen considerable advancements. While these methods are generally reliable, alternative approaches have also been explored. For example, Khan et al. [11] used the natural transform decomposition method to achieve more accurate solutions for parabolic and hyperbolic PDEs. Further improvements include a sixth-order compact scheme for the Helmholtz equation developed by Kumar and Dubey [12], the non-local operator method employed by Ren et al. [13], and the analytical solution for linear Fractional PDEs derived using the Fractional Fourier Transform by Mahae et al. [14]. Recent advancements have integrated deep learning with numerical methods for solving PDEs. Uriarte et al. [15] developed a deep learning scheme based on the finite element method, expanding the scope of computational techniques. Subsequently, Zheng et al. [16] explored the stochastic finite element method, while Gao et al. [10] applied the finite line method to PDE solutions. More recently, Saadeh et al. [17] introduced the Double Laplace Formable Transform Method, further enhancing the analytical and numerical approaches to solving PDEs. Some of the other newly developed numerical methods as well as analysis on PDE can be observed in [18]–[21]. These continuous developments highlight the growing sophistication of computational techniques in addressing complex partial differential equations.

Introduced by Grossman and Morlet in 1984, wavelet analysis has become a powerful mathematical tool with unique properties, including vanishing moments, wavelet decomposition, multiresolution analysis, localization, fast wavelet transform, and data compression. Its broad applicability spans signal analysis, DNA fingerprinting, image processing, and, more recently, numerical analysis.

Wavelets have proven particularly effective in solving numerical problems related to calculus, often surpassing traditional methods. The foundational work of Stephan Mallat and Yves Meyer established the basis for wavelet theory, particularly in the area of multiresolution analysis. This has spurred considerable research interest and a wealth of publications. Within the diverse family of wavelets, Haar wavelets are notable for their simplicity and clear analytical representation and have found application in the analysis of complex fluid dynamics, as demonstrated by Karkera et al. [22] in their study of the general unified MHD boundary-layer flow of a viscous fluid. The development of compactly supported wavelets by Daubechies [23] revolutionized wavelet theory, spurring considerable research and innovation. For instance, Mouley et al. [24] leveraged Daubechies wavelets to investigate the interaction between a finite crack and a shear wave, solving the resulting Fredholm integral equation derived from the governing shear wave equation via Fourier and Abel transformations. More recently, Legendre wavelets have been employed by Hussain et al. [25] to solve nonlinear hyperbolic equations.

Haar functions, originating with the Hungarian mathematician Alfred Haar [26] in 1910, have found widespread application across diverse fields. Their recognition in the 1980s as equivalent to the Daubechies wavelet of order 1 established a crucial connection between these two significant mathematical constructs. Characterized by their piecewise constant nature, Haar wavelets represent the simplest orthonormal wavelets with compact support. Despite their advantages, the inherent discontinuity of Haar wavelets presents challenges for direct application in solving differential equations. Two primary strategies have been developed to address this limitation. The first involves regularization using interpolating splines, such as B-splines or Deslaurier-Dabuc interpolating wavelets, as explored by Cattani [27]. The second approach, pioneered by Chen and Hsiao [28], utilizes an integral method. Chen and Hsiao's foundational work on Haar wavelet analysis in dynamical systems introduced the Haar operational matrix for integrating Haar function vectors. Building upon this, Hsiao [29] further contributed by developing a Haar product matrix and coefficient matrix, enabling the state analysis of linear time-delayed systems using Haar wavelets. Later, Lepik [30]–[32] advanced the field by developing a Haar wavelet method for solving ordinary and partial differential equations. Further expanding on this approach, Shi et al. [33], [34] introduced a novel numerical scheme utilizing a Scale-2 Haar wavelet (HW) and demonstrating its efficacy on both regular and irregular domains. Meanwhile, Hariharan and Kannan [35] performed a comparative analysis of the Haar wavelet method against the Restrictive Taylor's Series Method (RTSM) for solving convection-diffusion equations, ultimately establishing the superior performance of the Haar wavelet approach.

This study explores the solution of elliptic PDEs using Scale-3 HW, an advanced wavelet framework distinguished by its symmetric and antisymmetric properties, initially developed by Mittal and Pandit [36], [37]. Scale-3 HW has garnered considerable attention among mathematicians and engineers for its effectiveness in solving a wide range of functional equations, including ODEs, PDEs, and integro-differential equations [36], [38], [39]. The proposed approach formulates the solution as an infinite series that exhibits rapid convergence, ensuring high accuracy. The numerical results are then rigorously validated through comparison with both Scale-2 HW solutions and exact solutions, further substantiating the reliability and robustness of the proposed method.

To ensure the clarity and logical flow of the present work, this paper is structured as follows: Section 2 provides essential background on the Scale-2 Haar Wavelets. Sections 3 and 4 provide a detailed exploration of the theoretical framework underlying the operational matrix of Scale-3 HW and their application to function approximation. Section 5 introduces the Scale-3 HW methodology for solving two-dimensional elliptic partial differential equations that model steady-state heat distribution. Section 6 presents four numerical examples to demonstrate the efficacy of the proposed approach. Finally, Section 7 encapsulates the principal findings and conclusions drawn from this research.

II. Scale-2 Haar wavelets

Consider the interval $[A, B]$. Let J be the maximum resolution level. Define $M = 2^J$ and the sub-interval length $\Delta t = \frac{B-A}{2M}$. The dilation parameter j ranging from 0 to J determines the level of compression, while the translation parameter k ranging from 0 to $m-1$ shifts the wavelet's position within the interval. Here $m = 2^j$ and $i = m+k+1$ is the wavelet number. The first index $i = 1$ represents the Haar scaling function h_1, given by:

$$h_1(t) = \begin{cases} 1 & \text{for } t \in [A, B) \\ 0 & \text{otherwise.} \end{cases} \tag{2}$$

Further, when $m = 1$ and $k = 0$, the index $i = 2$ represents the Haar mother wavelet. The subsequent wavelets can be identified by:

$$h_i(t) = \begin{cases} 1 & \text{for } t \in [\varsigma_1(i), \varsigma_2(i)) \\ -1 & \text{for } t \in [\varsigma_2(i), \varsigma_3(i)) \\ 0 & \text{otherwise} \end{cases} \tag{3}$$

where

$$\begin{aligned} \varsigma_1(i) &= A + 2k\mu\Delta t \\ \varsigma_2(i) &= A + (2k+1)\mu\Delta t \\ \varsigma_3(i) &= A + 2(k+1)\mu\Delta t \\ \mu &= \frac{M}{m} \end{aligned}$$

Figure 1 shows the first eight Haar wavelets at resolution level $J = 2$ in the interval $[0, 1]$. Table I gives the relationship between dilation and translation parameters to indicate the wavelet number.

To address an r^{th} order differential equation, the subsequent integral of Haar function are used, which is defined as follows:

$$\begin{aligned} p_{r,i}(t) &= \int_A^t \int_A^t \cdots \int_A^t h_i(z) dz^r \\ &= \frac{1}{(r-1)!} \int_A^t (t-z)^{r-1} h_i(z) dz \end{aligned} \tag{4}$$

TABLE I: Index generation for Scale-2 Haar basis functions

j	0	1	1	2	2	2	2	3	3	3	3	3	3	3	3
$m = 2^j$	1	2	2	4	4	4	4	8	8	8	8	8	8	8	8
k	0	0	1	0	1	2	3	0	1	2	3	4	5	6	7
$i = m + k + 1$	2	3	4	5	6	7	8	9	10	11	12	13	14	15	16

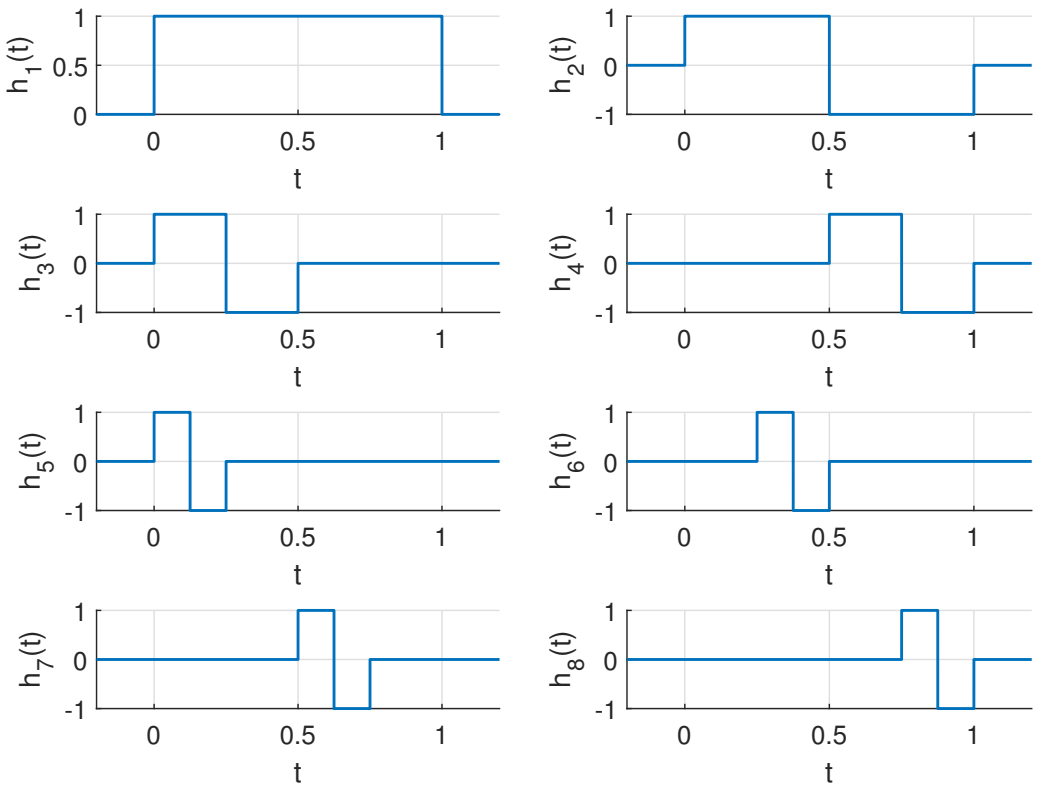

Fig. 1: The first eight Haar wavelets at resolution level $J = 2$.

The explicit form of $p_{r,i}(t)$ for $i = 2, 3, \ldots, 2M$ is given by

$$p_{r,i}(t) = \begin{cases} 0 \\ \text{for } t < \varsigma_1(i) \\ \\ \frac{1}{r!}(t - \varsigma_1(i))^r \\ \text{for } t \in [\varsigma_1(i), \varsigma_2(i)) \\ \\ \frac{1}{r!}\left\{(t - \varsigma_1(i))^r - 2(t - \varsigma_2(i))^r\right\} \\ \text{for } t \in [\varsigma_2(i), \varsigma_3(i)) \\ \\ \frac{1}{r!}\left\{(t - \varsigma_1(i))^r - 2(t - \varsigma_2(i))^r + (t - \varsigma_3(i))^r\right\} \\ \text{for } t > \varsigma_3(i) \end{cases} \tag{5}$$

For the case $i = 1$ with $\varsigma_1 = A$, $\varsigma_2 = \varsigma_3 = B$, we have

$$p_{r,1}(t) = \frac{1}{r!}(t - A)^r. \tag{6}$$

III. Scale-3 Haar wavelets

For any $s \in [A, B]$ with maximal resolution level J, define $M = 3^J$ and sub-interval length as $\Delta s = \frac{B-A}{3M}$. Let $j = 0, 1, 2, \ldots, J$ be the dilation parameter, $k = 0, 1, 2, \ldots, m-1$ be the translation parameter, where $m = 3^j$ and index i gives the relation between m and k. The initial index value, $i = 1$ is assigned for scaling function defined as

$$h_1(s) = \begin{cases} 1 & \text{for } s \in [A, B) \\ 0 & \text{otherwise.} \end{cases} \tag{7}$$

For indices $i > 1$, even indices ($i = m + 2k + 1$) correspond to symmetric wavelets, denoted by $\psi^{(1)}(s)$, while odd indices ($i = m + 2k + 2$) represent antisymmetric wavelets, denoted by $\psi^{(2)}(s)$. Both are defined in function form as:

$$\psi_i^{(1)}(s) = \frac{1}{\sqrt{2}} \begin{cases} -1 & \text{for } s \in [\kappa(i), \lambda(i)) \\ 2 & \text{for } s \in [\lambda(i), \eta(i)) \\ -1 & \text{for } s \in [\eta(i), \theta(i)) \end{cases} \tag{8}$$

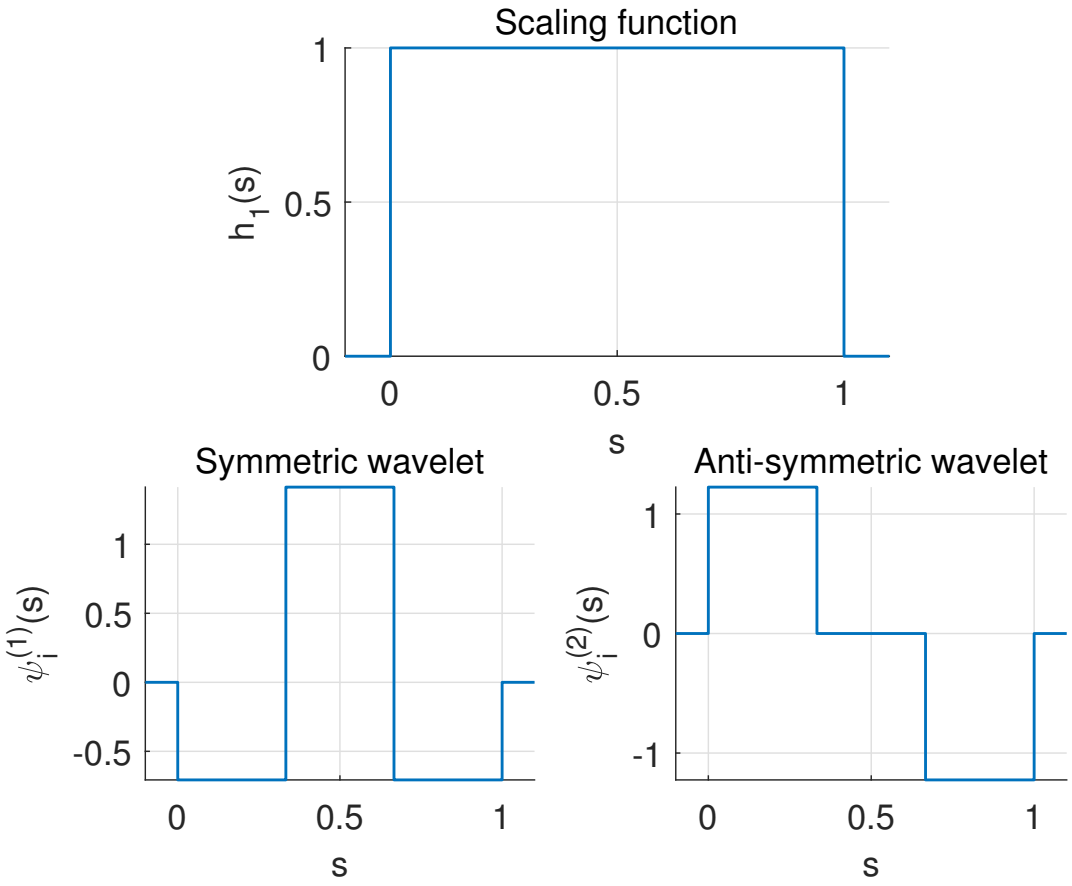

Fig. 2: Scaling, symmetric and anti-symmetric wavelets of Scale-3 HW.

$$\psi_i^{(2)}(s) = \sqrt{\frac{3}{2}} \begin{cases} 1 & \text{for } s \in [\kappa(i), \lambda(i)) \\ 0 & \text{for } s \in [\lambda(i), \eta(i)) \\ -1 & \text{for } s \in [\eta(i), \theta(i)) \end{cases} \tag{9}$$

where

$$\kappa(i) = A + (B-A)\frac{k}{m}$$
$$\lambda(i) = A + (B-A)\frac{3k+1}{3m}$$
$$\eta(i) = A + (B-A)\frac{3k+2}{3m}$$
$$\theta(i) = A + (B-A)\frac{k+1}{m}$$

Pictorial representation of Scale-3 HW for $i = 1, 2, 3$ is plotted in Figure 2.

The solution of an r^{th} order differential equation requires integrals of above Scale-3 HW function which are given by

$$p_{r,1}(s) = \begin{cases} \frac{(s-A)^r}{r!} & \text{for } s \in [A, B) \\ 0 & \text{otherwise} \end{cases} \tag{10}$$

$$\psi_{r,i}^{(1)}(s) = \frac{1}{\sqrt{2}} \begin{cases} \frac{-(s-\kappa(i))^r}{r!} \\ \text{for } s \in [\kappa(i), \lambda(i)) \\ \frac{-(s-\kappa(i))^r + 3(s-\lambda(i))^r}{r!} \\ \text{for } s \in [\lambda(i), \eta(i)) \\ \frac{-(s-\kappa(i))^r + 3(s-\lambda(i))^r - 3(s-\eta(i))^r}{r!} \\ \text{for } s \in [\eta(i), \theta(i)) \\ \frac{-(s-\kappa(i))^r + 3(s-\lambda(i))^r - 3(s-\eta(i))^r + (s-\theta(i))^r}{r!} \\ \text{for } s \in [\theta(i), B) \end{cases} \tag{11}$$

$$\psi_{r,i}^{(2)}(s) = \sqrt{\frac{3}{2}} \begin{cases} \frac{(s-\kappa(i))^r}{r!} \\ \text{for } s \in [\kappa(i), \lambda(i)) \\ \frac{(s-\kappa(i))^r - (s-\lambda(i))^r}{r!} \\ \text{for } s \in [\lambda(i), \eta(i)) \\ \frac{(s-\kappa(i))^r - (s-\lambda(i))^r - (s-\eta(i))^r}{r!} \\ \text{for } s \in [\eta(i), \theta(i)) \\ \frac{(s-\kappa(i))^r - (s-\lambda(i))^r - (s-\eta(i))^r + (s-\theta(i))^r}{r!} \\ \text{for } s \in [\theta(i), B) \end{cases} \tag{12}$$

IV. Function approximation with associated Haar matrix

The orthogonality of Scale-3 Haar wavelets allows any square-integrable function $f(s)$ defined on the interval $[0, 1)$ to be expressed as an infinite series, a linear combination of Scale-3 HW basis functions given by,

$$f(s) = c_1 h_1 + \sum_{i-even\ index}^{\infty} c_i \psi_i^{(1)}(s) + \sum_{i-odd\ index}^{\infty} c_i \psi_i^{(2)}(s) \tag{13}$$

When $f(s)$ is piecewise constant or can be approximated as such within each sub-interval, its series expansion can be truncated to a finite number of terms, effectively yielding a finite representation, that is,

$$\begin{aligned} f(s) &= c_1 h_1 + \sum_{i-even\ index}^{3M} c_i \psi_i^{(1)}(s) + \sum_{i-odd\ index}^{3M} c_i \psi_i^{(2)}(s) \\ &= \mathbf{c}^T H_{3M} \end{aligned}$$

where $M = 3^J$ and J represent the maximal resolution level. The notation $\mathbf{c}^T$ is adopted to signify the $3M$-dimensional row vector, facilitating the representation of Haar wavelet coefficients $[c_1, \ldots, c_{3M}]$ whereas H_{3M} denotes the Haar wavelet operational matrix of order $3M \times 3M$, $H_{3M} = [h_1(s), \psi_2^{(1)}(s), \psi_3^{(2)}(s), \ldots, \psi_{3M-1}^{(1)}(s), \psi_{3M}^{(2)}(s)]$. For instance the Haar operational matrix corresponding to $J = 0, m = 1$ is 3×3 matrix given by,

$$H_{3M}(s) = \begin{bmatrix} 1 & 1 & 1 \\ -0.7071 & 1.4142 & -0.7071 \\ 1.2247 & 0 & -1.2247 \end{bmatrix}_{3\times 3}$$

As H_{3M} is an orthogonal matrix, it follows directly that $\mathbf{c}^T = f(s) H_{3M}^T(s)$ where the superscript T indicates transpose operator.

V. Method of solution for elliptic PDE

Consider a steady-state heat distribution equation with a heat source term $g(x, y)$ as

$$\frac{\partial^2 u}{\partial x^2} + \frac{\partial^2 u}{\partial y^2} = g(x, y) \qquad (x, y) \in [A, B] \times [A, B] \tag{14}$$

subject to specified initial and boundary conditions. Utilizing the Scale-3 HW basis, we approximate the solution, $u(x, y)$, and its partial derivatives. The approximation process begins by fixing the variable y and performing the discretization along grid lines parallel to the x-axis, which is given as follows,

$$\frac{\partial^2 u(x)}{\partial x^2} = c_1 h_1 + \sum_{i-even}^{3M} c_i \psi_i^{(1)}(x) + \sum_{i-odd}^{3M} c_i \psi_i^{(2)}(x) \tag{15}$$

$$\frac{\partial u(x)}{\partial x} = \sum_{i=1}^{3M} c_i p_{1,i}(x) + \frac{\partial u(A)}{\partial x} \tag{16}$$

$$u(x) = \sum_{i=1}^{3M} c_i p_{2,i}(x) + \frac{\partial u(A)}{\partial x}(x - A) + u(A) \tag{17}$$

where $h_1(x)$, $\psi_i^{(1)}(x)$, $\psi_i^{(2)}(x)$ together constitute the Haar matrix and $p_{1,i}(x)$, $p_{2,i}(x)$ represent the Haar integral matrices. At the collocation points, equation (17) can be written in matrix form as,

$$u(x_l) = \begin{bmatrix} u(x_1) \\ u(x_2) \\ \vdots \\ u(x_{3m}) \end{bmatrix} = Q_1 \begin{bmatrix} c \\ b_1 \end{bmatrix} \tag{18}$$

where $c^T = (c_1, c_2, \ldots, c_{3M})$, $b_1^T = (\frac{\partial u(A)}{\partial x}, u(A))$ and

$$\underbrace{\begin{bmatrix} p_{2,1}(x_1) & p_{2,2}(x_1) & \cdots & p_{2,3M}(x_1) & x_1 - A & 1 \\ p_{2,1}(x_2) & p_{2,2}(x_2) & \cdots & p_{2,3M}(x_2) & x_2 - A & 1 \\ \vdots & \vdots & \ddots & \vdots & \vdots & \vdots \\ p_{2,1}(x_{3M}) & p_{2,2}(x_{3M}) & \cdots & p_{2,3M}(x_{3M}) & x_{3M} - A & 1 \end{bmatrix}}_{Q_1}$$

with Q_1 having dimension $3M \times (3M + 2)$. The boundary conditions associated with the given problem may be either Dirichlet or Neumann, which can be easily tackled by this Scale-3 HW approach as follows:

1. *Dirichlet boundary condition*: Using equation (17), the additional two equations for boundary conditions are

$$f_{ex1} = \begin{bmatrix} u(A) \\ u(B) \end{bmatrix} \tag{19}$$

$$= Q_2 \begin{bmatrix} c \\ b_1 \end{bmatrix} \tag{20}$$

where

$$Q_2 = \begin{bmatrix} p_{2,1}(A) & p_{2,2}(A) & \cdots & p_{2,3M}(A) & 0 & 1 \\ p_{2,1}(B) & p_{2,2}(B) & \cdots & p_{2,3M}(B) & B - A & 1 \end{bmatrix}$$

with Q_2 having dimension $2 \times (3M + 2)$.

2. *Neumann boundary condition*: Using equation (16)

$$f_{\overline{ex1}} = \begin{bmatrix} u'(A) \\ u'(B) \end{bmatrix} \tag{21}$$

$$= \overline{Q_2} \begin{bmatrix} c \\ b_1 \end{bmatrix} \tag{22}$$

where

$$\overline{Q_2} = \begin{bmatrix} p_{1,1}(A) & p_{1,2}(A) & \cdots & p_{1,3M}(A) & 1 & 0 \\ p_{1,1}(B) & p_{1,2}(B) & \cdots & p_{1,3M}(B) & 1 & 0 \end{bmatrix}$$

with $\overline{Q_2}$ having dimension $2 \times (3M + 2)$.

Combining equation (18) and (20) and substituting for $\begin{bmatrix} c \\ b_1 \end{bmatrix}$ in equation (15), we get

$$\begin{bmatrix} \frac{\partial^2 u(x_1)}{\partial x^2} & \cdots & \frac{\partial^2 u(x_{3M})}{\partial x^2} \end{bmatrix}^T = \begin{bmatrix} H^T & 0 & 0 \end{bmatrix} W^{-1} \begin{bmatrix} u \\ f_{ex1} \end{bmatrix} \tag{23}$$

$$\frac{\partial^2 u}{\partial x^2} = \hat{H} W^{-1} \begin{bmatrix} u \\ f_{ex1} \end{bmatrix} = B_1 u + B_2 f_{ex1} \tag{24}$$

where $W = \begin{bmatrix} Q_1 \\ Q_2 \end{bmatrix}$, $\hat{H} = \begin{bmatrix} H^T & 0 & 0 \end{bmatrix}$ and specifically, B_1 and B_2 denote matrices constructed from the first M columns and the last two columns, respectively, of the matrix $\hat{H} W^{-1}$. The approximation of $\frac{\partial^2 u(x_l)}{\partial x^2}$ can be extended from 1D to 2D domain by making use of Kronecker tensor product as

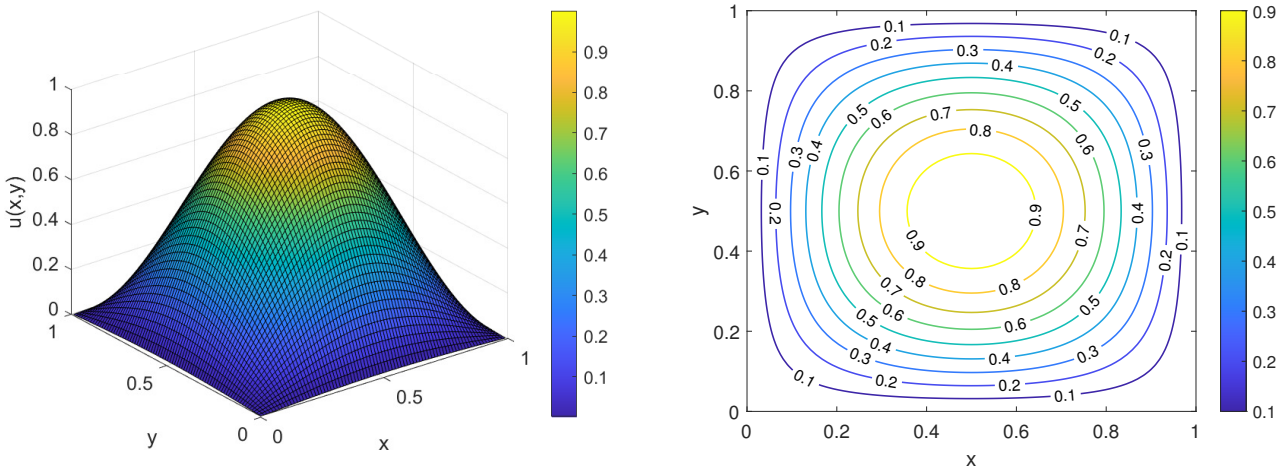

(a) Surface plot. (b) Contour plot.

Fig. 3: Scale-3 HW solution plot at resolution level $J = 3$ for Problem 1.

follows,

$$\frac{\partial^2 \mathbf{u}(\mathbf{x_l}, \mathbf{y_k})}{\partial \mathbf{x^2}} = (\mathbf{B_1} \otimes \mathbf{I_y})\mathbf{u}(\mathbf{x_l}, \mathbf{y_k}) + (\mathbf{B_2} \otimes \mathbf{I_y})\mathbf{f_1} \quad (25)$$

$$= \mathbf{D_x}\mathbf{u}(\mathbf{x_l}, \mathbf{y_k}) + \mathbf{k_x} \quad (26)$$

where $\mathbf{f_1}$ is $6M \times 1$ column vector, I_y is the identity matrix of order $3M \times 3M$, $\mathbf{u}^T = (u(x_1, y_1), \ldots, u(x_1, y_{3M}), u(x_2, y_1), \ldots, u(x_2, y_{3M}), \ldots, u(x_{3M}, y_1), \ldots, u(x_{3M}, y_{3M}))$ and $(\frac{\partial^2 \mathbf{u}}{\partial \mathbf{x^2}})^T = (\frac{\partial^2 u(x_1,y_1)}{\partial x^2}, \ldots, \frac{\partial^2 u(x_1,y_{3M})}{\partial x^2}, \frac{\partial^2 u(x_2,y_1)}{\partial x^2}, \ldots, \frac{\partial^2 u(x_2,y_{3M})}{\partial x^2}, \ldots, \frac{\partial^2 u(x_{3M},y_1)}{\partial x^2}, \ldots, \frac{\partial^2 u(x_{3M},y_{3M})}{\partial x^2})$. A similar procedure is carried out by fixing the variable x and approximating along the $y-$axis to get the final equation as

$$\frac{\partial^2 \mathbf{u}(\mathbf{x_l}, \mathbf{y_k})}{\partial \mathbf{y^2}} = (\mathbf{I_x} \otimes \mathbf{B_3})\mathbf{u}(\mathbf{x_l}, \mathbf{y_k}) + (\mathbf{I_x} \otimes \mathbf{B_4})\mathbf{f_2} \quad (27)$$

$$= \mathbf{D_y}\mathbf{u}(\mathbf{x_l}, \mathbf{y_k}) + \mathbf{k_y} \quad (28)$$

where $\mathbf{f_2}$ is $6M \times 1$ column vector, I_x is the identity matrix of order $3M \times 3M$.

On adding equations (26) and (28) and comparing it with equation (14) at 2D collocation points gives the following form,

$$(\mathbf{D_x} + \mathbf{D_y})\mathbf{u} = \mathbf{g}(\mathbf{x_l}, \mathbf{y_k}) - \mathbf{k_x} - \mathbf{k_y} \quad (29)$$

The system described in (29) is solved for u employing the Gauss-Seidel iterative scheme. To evaluate the efficacy and accuracy of the proposed methodology, few numerical problems are addressed. The precision of the results obtained at a specific resolution level J is assessed using error metrics, including the absolute error, L_∞ error and L_2 error with the following expressions:

$$\text{Absolute error} = |u_{num}(x_l, y_k) - u_{ex}(x_l, y_k)| \quad (30)$$

$$L_\infty = max_{1 \le k,l \le 3M} |u_{num}(x_l, y_k) - u_{ex}(x_l, y_k)| \quad (31)$$

$$L_2 = \frac{\sqrt{\sum_{l,k=1}^{3M} |u_{num}(x_l, y_k) - u_{ex}(x_l, y_k)|^2}}{\sqrt{\sum_{l,k=1}^{3M} |u_{ex}(x_l, y_k)|^2}} \quad (32)$$

where u_{num}, u_{ex} are the approximate and exact solutions respectively. The error bound is calculated by L_2 norm, given by

$$\| u_{ex}(x, y) - u_{num}(x, y) \|_{L_2} \le \frac{L}{9\sqrt{18}} \frac{1}{3^J} \quad (33)$$

Furthermore, as we increase the resolution level ($J \to \infty$), the error goes to zero, providing evidence that the method converges. Additionally, we have calculated the experimental order of convergence, $O_c(J)$, defined by

$$O_c(J) = \frac{log_e[L_\infty(J-1)] - log_e[L_\infty(J)]}{log_e 3} \quad (34)$$

VI. Results and Discussions

This section delineates the numerical outcomes of four illustrative problems, demonstrating the accuracy, versatility, and convergence properties of the proposed methods. A comparative evaluation against established methods from the literature underscores the efficacy of the novel Scale-3 Haar Wavelet approach. The algorithms were implemented using MATLAB 2023a, and executed on a system equipped with an Intel Core i3 processor and 16 GB of RAM.

A. Problem 1:

Consider the steady-state heat distribution equation, given as follows,

$$\frac{\partial^2 u}{\partial x^2} + \frac{\partial^2 u}{\partial y^2} = -2\pi^2 sin(\pi x) sin(\pi y) \qquad (x, y) \in [0, 1] \times [0, 1] \quad (35)$$

with $u(x, y) = 0$ on the boundaries having an analytical solution

$$u(x, y) = sin(\pi x) sin(\pi y). \quad (36)$$

Approximating the highest derivative along $x-$axis and $y-$axis separately, while keeping the other variable fixed, we get two equations as

$$u(x) = \sum_{i=1}^{3M} c_i p_{2,i}(x) + \frac{\partial u(0)}{\partial x}(x) + u(0) \quad (37)$$

$$u(y) = \sum_{i=1}^{3M} d_i p_{2,i}(y) + \frac{\partial u(0)}{\partial y}(y) + u(0) \quad (38)$$

TABLE II: Comparison of Scale-3 HWM with Scale-2 HWM and FDM for Problem 1.

J	Scale-2 HW			FDM			Scale-3 HW			Order of convergence (O_c)	
	No. of Points	L_2	L_∞	No. of Points	L_2	L_∞	No. of Points	L_2	L_∞	Scale-2 HW	Scale-3 HW
1	4	0.0241	0.0206	9	0.013	0.013	9	0.0050	0.0050	-	-
2	8	0.0063	0.0061	27	0.0012	0.0012	27	5.6334E-04	5.6334E-04	1.7558	1.9873
3	16	0.0016	0.0016	81	1.2852E-04	1.2852E-04	81	6.2669E-05	6.2669E-05	1.9307	1.9989
4	32	4.0121E-04	4.0024E-04	-	-	-	-	-	-	1.9991	-
5	64	1.0037E-04	1.0031E-04	-	-	-	-	-	-	1.9964	-
6	128	2.5098E-05	2.5094E-05	-	-	-	-	-	-	1.9991	-

TABLE III: Time comparison in Problem 1.

J	Scale-2 HW		FDM		Scale-3 HW	
	No. of Points	CPU Time (s)	No. of Points	CPU Time (s)	No. of Points	CPU Time (s)
1	4	0.0156	9	0.0312	9	0.0156
2	8	0.0156	27	0.0781	27	0.0625
3	16	0.0312	81	6.5781	81	4.5156
4	32	0.1875	-	-	-	-
5	64	1.9062	-	-	-	-
6	128	67.625	-	-	-	-

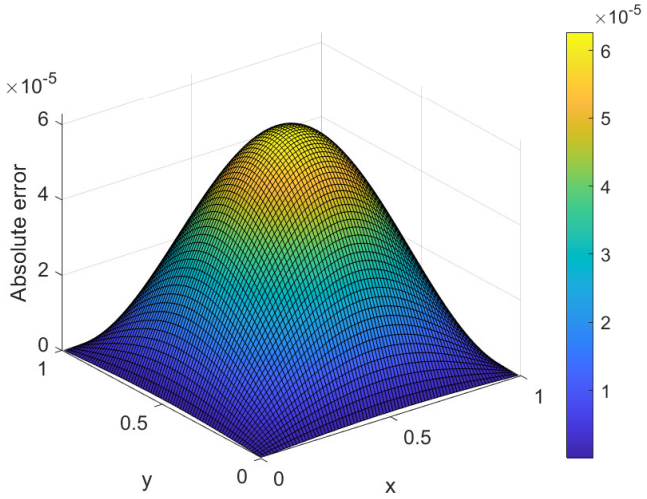

Fig. 4: Absolute error plot at resolution level $J = 3$ for Problem 1.

Using given boundary conditions, the additional equations can be written as

$$f_{ex1} = \begin{bmatrix} p_{2,1}(0) & p_{2,2}(0) & \cdots & p_{2,3M}(0) & 0 & 1 \\ p_{2,1}(1) & p_{2,2}(1) & \cdots & p_{2,3M}(1) & 1 & 1 \end{bmatrix} \begin{bmatrix} c \\ b_1 \end{bmatrix} \tag{39}$$

$$f_{ex2} = \begin{bmatrix} p_{2,1}(0) & p_{2,2}(0) & \cdots & p_{2,3M}(0) & 0 & 1 \\ p_{2,1}(1) & p_{2,2}(1) & \cdots & p_{2,3M}(1) & 1 & 1 \end{bmatrix} \begin{bmatrix} d \\ b_2 \end{bmatrix} \tag{40}$$

where $c^T = (c_1, c_2, \ldots, c_{3M})$, $d^T = (d_1, d_2, \ldots, d_{3M})$ are Haar coefficients along x and y directions respectively, and $b_1^T = (\frac{\partial u(0)}{\partial x}, u(0))$, $b_2^T = (\frac{\partial u(0)}{\partial y}, u(0))$. After extending the approximation to the 2D domain we get,

$$\begin{aligned} \frac{\partial^2 \mathbf{u}(\mathbf{x_l}, \mathbf{y_k})}{\partial \mathbf{x^2}} &= (\mathbf{B_1} \otimes \mathbf{I_y})\mathbf{u}(\mathbf{x_l}, \mathbf{y_k}) + (\mathbf{B_2} \otimes \mathbf{I_y})\mathbf{f_1} \\ &= \mathbf{D_x}\mathbf{u}(\mathbf{x_l}, \mathbf{y_k}) + \mathbf{k_x} \end{aligned}$$

$$\begin{aligned} \frac{\partial^2 \mathbf{u}(\mathbf{x_l}, \mathbf{y_k})}{\partial \mathbf{y^2}} &= (\mathbf{I_x} \otimes \mathbf{B_3})\mathbf{u}(\mathbf{x_l}, \mathbf{y_k}) + (\mathbf{I_x} \otimes \mathbf{B_4})\mathbf{f_2} \\ &= \mathbf{D_y}\mathbf{u}(\mathbf{x_l}, \mathbf{y_k}) + \mathbf{k_y} \end{aligned}$$

where $\mathbf{f_1}, \mathbf{f_2}$ are zero vectors of dimension $6M \times 1$. On adding above two equations we get,

$$(\mathbf{D_x} + \mathbf{D_y})\mathbf{u} = -2\pi^2 sin(\pi \mathbf{x_l}) sin(\pi \mathbf{y_k}) - \mathbf{k_x} - \mathbf{k_y} \tag{41}$$

The system is solved for $\mathbf{u}$ using the Gauss-Seidel iterative method. The maximum absolute error (L_∞) and L_2 error are computed, tabulated in Table II, and compared with the results obtained from the Scale-2 HW method and the existing numerical scheme, Finite Difference Method. Although both the Scale-2 HW and Scale-3 HW methods exhibit quadratic convergence, as evidenced in Table II, the Scale-3 HW method demonstrates superior accuracy with minimal error at lower resolution levels. Specifically, the accuracy achieved at $J = 6$ with 128 collocation points using the Scale-2 HW method is nearly matched by the Scale-3 HW method at $J = 3$ with only 81 collocation points, while requiring significantly less computational time, as detailed in Table III. Furthermore, the CPU time for the Scale-3 HW method is notably lower than that of FDM for the same number of collocation points, underscoring the enhanced efficiency and accuracy of the Scale-3 HW approach over both Scale-2 HW and FDM. Table IV provides a comparison of the numerical and exact solutions at selected collocation points. The solution is visualized through 3D plot and contour plot in Figures 3a and 3b, while Figure 4 illustrates the absolute error plot at resolution level $J = 3$. The color variation in Figure 4 illustrates the distribution of errors across different points, with lighter shades indicating higher errors and darker shades representing lower errors.

B. Problem 2:

Consider

$$\frac{\partial^2 u}{\partial x^2} + \frac{\partial^2 u}{\partial y^2} = xe^y \qquad (x, y) \in [0, 1] \times [0, 1] \tag{42}$$

The boundary conditions associated with this equation are $u(0, y) = 0$, $u(1, y) = e^y$, $u(x, 0) = x$ and $u(x, 1) = xe$. The aforementioned steady-state heat distribution equation

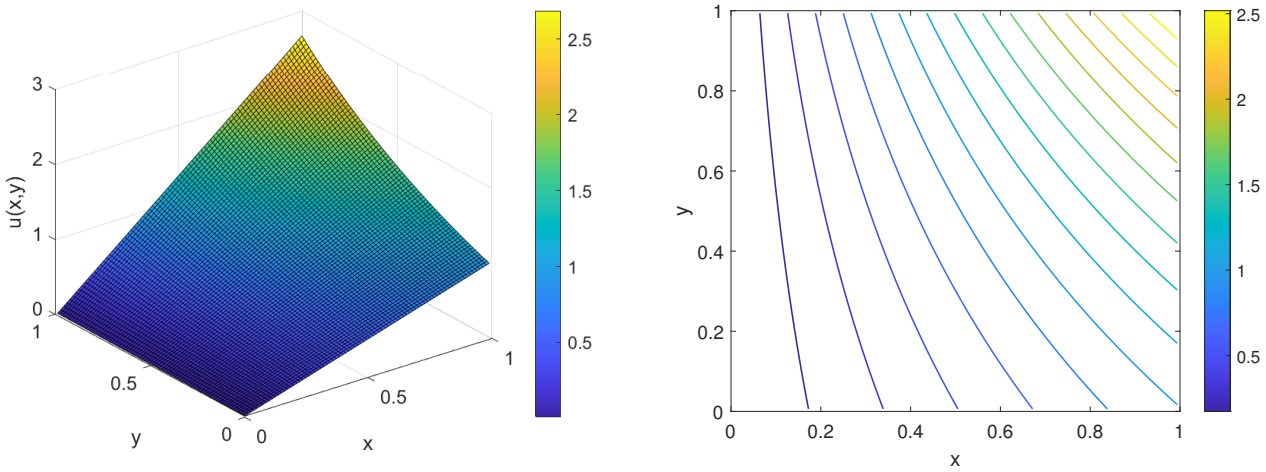

(a) Surface plot. (b) Contour plot.

Fig. 5: Scale-3 HW solution plot at resolution level $J = 3$ for Problem 2.

TABLE IV: Numerical and exact solution at selected collocation points for Problem 1 at $J = 3$.

Selected collocation points	Scale-3 HW solution	Exact solution
$\left(\frac{40.5}{81}, \frac{40.5}{81}\right)$	0.999937	1.000000
$\left(\frac{8.5}{81}, \frac{8.5}{81}\right)$	0.104797	0.104804
$\left(\frac{24.5}{81}, \frac{8.5}{81}\right)$	0.263358	0.263374
$\left(\frac{76.5}{81}, \frac{6.5}{81}\right)$	0.0433123	0.043315
$\left(\frac{1.5}{81}, \frac{79.5}{81}\right)$	0.0033806	0.0033808
$\left(\frac{45.5}{81}, \frac{77.5}{81}\right)$	0.132786	0.132795
$\left(\frac{65.5}{81}, \frac{58.5}{81}\right)$	0.433253	0.43328
$\left(\frac{14.5}{81}, \frac{55.5}{81}\right)$	0.445458	0.445486
$\left(\frac{27.5}{81}, \frac{32.5}{81}\right)$	0.833696	0.833748
$\left(\frac{58.5}{81}, \frac{41.5}{81}\right)$	0.76542	0.765468

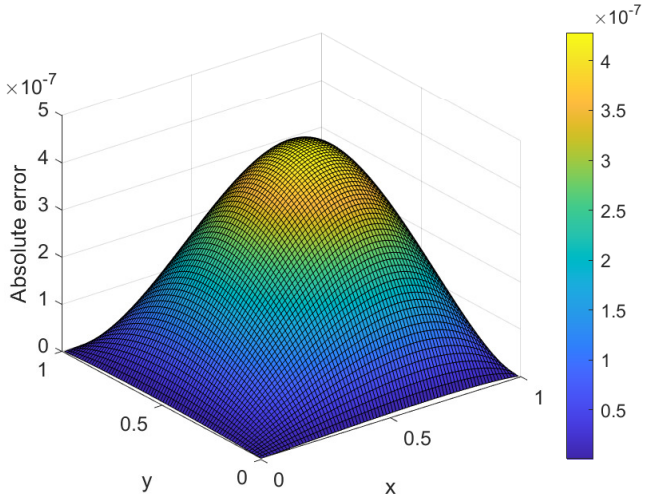

Fig. 6: Absolute error plot at resolution level $J = 3$ for Problem 2.

possesses an analytical solution given by

$$u(x, y) = xe^y. \tag{43}$$

The final extended approximation for the 2D domain using the Kronecker tensor product in both the x and y directions are as follows:

$$\begin{aligned}\frac{\partial^2 \mathbf{u}(\mathbf{x_l}, \mathbf{y_k})}{\partial \mathbf{x^2}} &= (\mathbf{B_1} \otimes \mathbf{I_y})\mathbf{u}(\mathbf{x_l}, \mathbf{y_k}) + (\mathbf{B_2} \otimes \mathbf{I_y})\mathbf{f_1} \\ &= \mathbf{D_x}\mathbf{u}(\mathbf{x_l}, \mathbf{y_k}) + \mathbf{k_x}\end{aligned}$$

$$\begin{aligned}\frac{\partial^2 \mathbf{u}(\mathbf{x_l}, \mathbf{y_k})}{\partial \mathbf{y^2}} &= (\mathbf{I_x} \otimes \mathbf{B_3})\mathbf{u}(\mathbf{x_l}, \mathbf{y_k}) + (\mathbf{I_x} \otimes \mathbf{B_4})\mathbf{f_2} \\ &= \mathbf{D_y}\mathbf{u}(\mathbf{x_l}, \mathbf{y_k}) + \mathbf{k_y}\end{aligned}$$

Here the $\mathbf{f_1}$ and $\mathbf{f_2}$ are non zero $6M \times 1$ column vectors given by

$$\mathbf{f_1}^T = (\underbrace{0, \ldots, 0}_{3^{J+1}\ times}, e^{x_1}, \ldots, e^{x_{3M}})$$

$$\mathbf{f_2}^T = (y_1, y_1 e, y_2, y_2 e, \ldots, y_{3M}, y_{3M} e)$$

whereas the vectors were zero in Problem 1. On adding above two equations we get,

$$(\mathbf{D_x} + \mathbf{D_y})\mathbf{u} = \mathbf{x_l}\mathbf{e_k^y} - \mathbf{k_x} - \mathbf{k_y} \tag{44}$$

and the system of equations is solved to determine u. Although both methods yield stable and acceptably accurate solutions, it is evident that the approximate solution converges at a faster rate with the Scale-3 HW method compared to the Scale-2 HW method. The corresponding solution (3D and contour) and absolute error plots at resolution level $J = 3$ are presented in Figures 5a and 5b and Figure 6, respectively. The color variation in Figure 6 illustrates the distribution of errors across different points, with lighter shades indicating higher errors and darker shades representing lower errors. A comparison of the numerical and exact solutions is provided in Table V, while Table VI highlights the L_∞ and L_2 error comparisons between the FDM and the Scale-3 HW method. For various resolution levels $J = 1, 2, \ldots, 6$, the accuracy of the proposed method is evaluated and compared with the Scale-2 HW method. The results are graphically represented in Figure 7. Additionally, logarithmic plots of the maximum absolute errors for

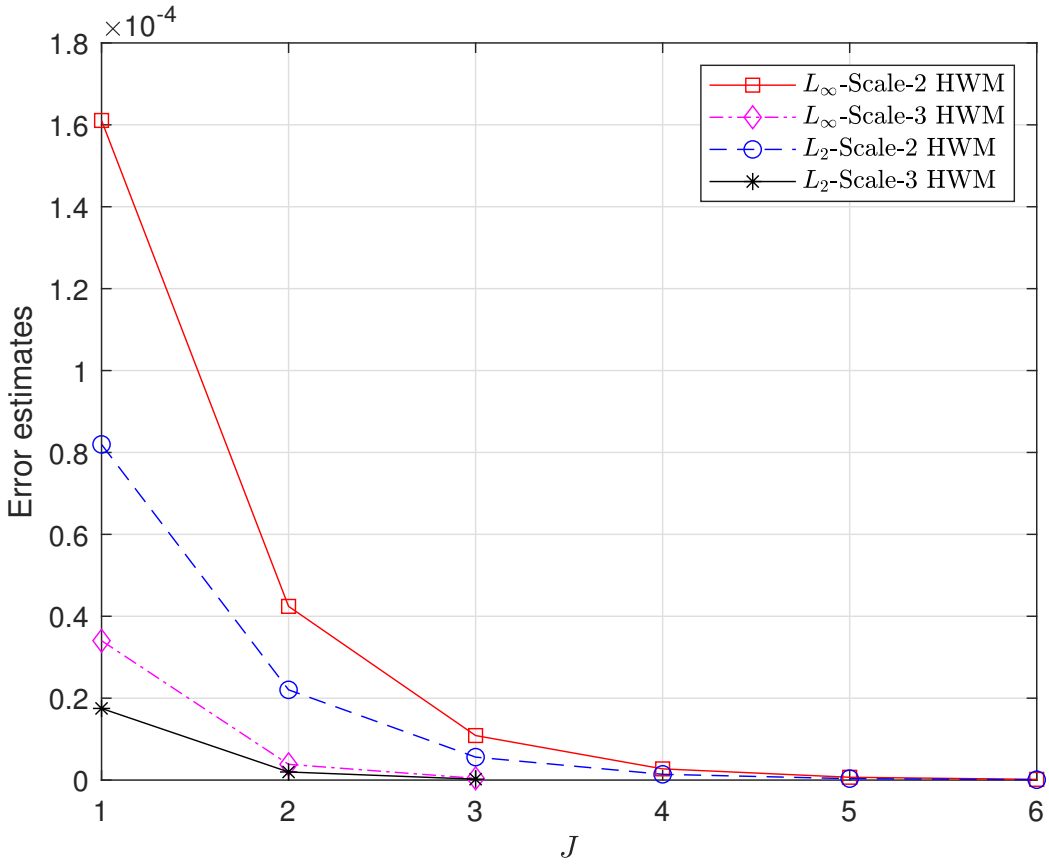

Fig. 7: Error estimates at different resolution levels for Problem 2.

different J values, as shown in Figure 8, demonstrate the order of convergence of the Scale-2 HW and Scale-3 HW methods.

TABLE V: Numerical and Exact solution at some collocation points for Problem 2 at $J = 3$.

Selected collocation points	Scale-3 HW solution	Exact solution
$\left(\frac{40.5}{81}, \frac{40.5}{81}\right)$	0.82436	0.824361
$\left(\frac{8.5}{81}, \frac{8.5}{81}\right)$	0.116549	0.116549
$\left(\frac{24.5}{81}, \frac{8.5}{81}\right)$	0.335935	0.335935
$\left(\frac{76.5}{81}, \frac{6.5}{81}\right)$	1.02336	1.02336
$\left(\frac{1.5}{81}, \frac{79.5}{81}\right)$	0.049415	0.049415
$\left(\frac{45.5}{81}, \frac{77.5}{81}\right)$	1.46236	1.46236
$\left(\frac{65.5}{81}, \frac{58.5}{81}\right)$	1.665	1.665
$\left(\frac{14.5}{81}, \frac{55.5}{81}\right)$	0.355185	0.355185
$\left(\frac{27.5}{81}, \frac{32.5}{81}\right)$	0.507109	0.507109
$\left(\frac{58.5}{81}, \frac{41.5}{81}\right)$	1.20553	1.20553

C. *Problem 3:*

Consider steady-state heat distribution equation with sinusoidal heat source vector

$$\frac{\partial^2 u}{\partial x^2} + \frac{\partial^2 u}{\partial y^2} = sin(\pi x) \qquad (x, y) \in [0, 1] \times [0, 1] \quad (45)$$

Applying the proposed scheme to the current problem yields an approximate solution that is well close to the closed-form solution

$$u(x, y) = \frac{sin(\pi x)}{\pi^2 sinh(\pi)}(sinh(\pi y) + sinh(\pi(1-y)) - sinh(\pi)) \quad (46)$$

The Dirichlet boundary conditions are derived from the given analytical solution. After applying all approximations, the final system of equations is given by

$$(\mathbf{D_x} + \mathbf{D_y})\mathbf{u} = sin(\pi \mathbf{x_l}) - \mathbf{k_x} - \mathbf{k_y} \quad (47)$$

This system is then solved to determine u. The simulation results are visualized graphically, with Figures 9a and 9b displaying the Scale-3 HW solution surface plot as well as contour plot. As observed in Figures 10 and 12, the proposed method demonstrates higher accuracy and lower computational error compared to the Scale-2 HW method. The color variations in Figures 10 and 11 represent the error distribution at different collocation points, where lighter colors indicate higher errors and darker colors signify lower errors. The Scale-3 HW and exact solutions are presented in Table VII. Table VIII compares the Finite Difference Method with the Scale-3 HW method in terms of maximum absolute error and L_2 error, highlighting the superiority of Scale-3 HW over FDM. Additionally, the logarithmic plot in Figure 13 confirms the quadratic convergence of the Scale-2 and Scale-3 HW methods toward the solution.

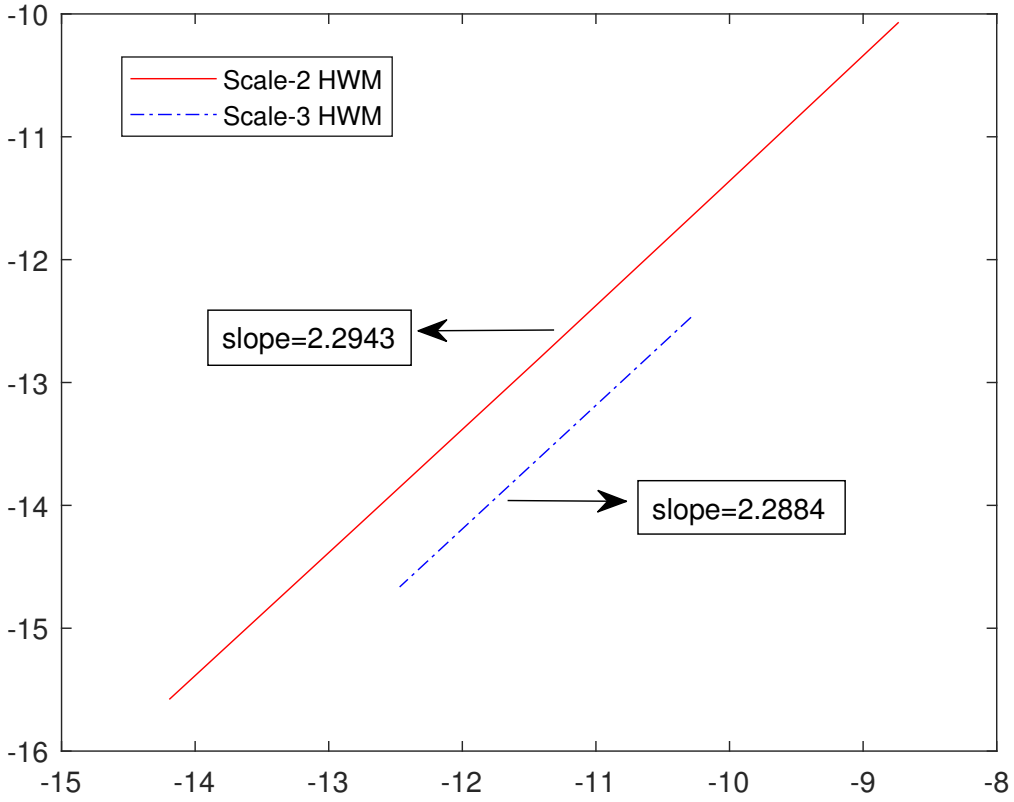

Fig. 8: Numerical order of convergence for Problem 2 using $log - log$ plot.

TABLE VI: Evaluation of the numerical accuracy of Scale-3 HWM and FDM solutions for Problem 2.

Points	L_∞		L_2	
	FDM	Scale3 HW	FDM	Scale3 HW
9	8.5906E-05	3.4037E-05	3.7594E-05	1.7497E-05
27	8.2942E-06	3.8433E-06	4.0436E-06	1.9761E-06
81	8.7744E-07	4.2796E-07	4.4320E-07	2.1996E-07

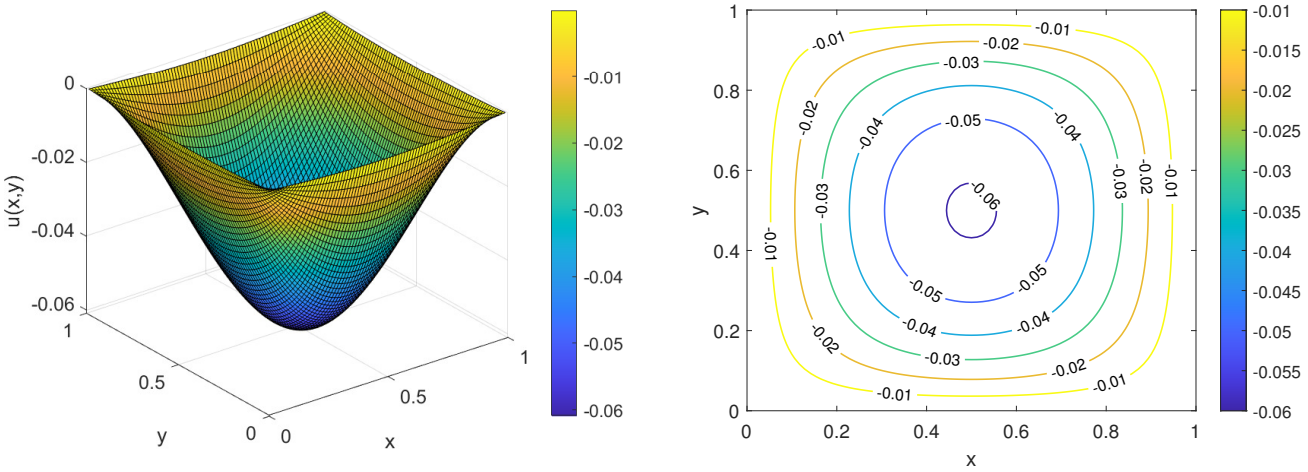

(a) Surface plot.

(b) Contour plot.

Fig. 9: Scale-3 HW solution plot at resolution level $J = 3$ for Problem 3.

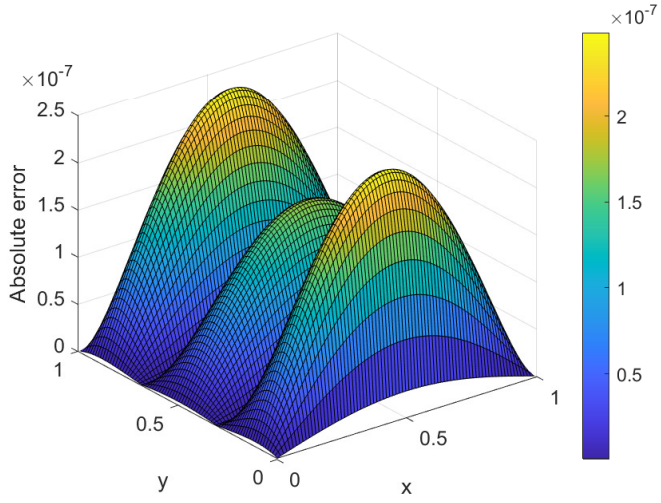

Fig. 10: Absolute error plot at resolution level $J = 3$ for Problem 3.

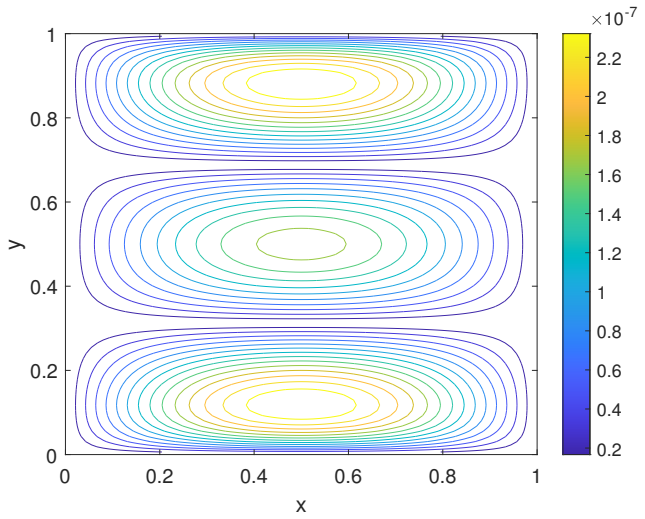

Fig. 11: Contour plot of absolute error at resolution level $J = 3$ for Problem 3.

TABLE VII: Numerical and exact solution at some collocation points for Problem 3 at $J = 3$.

Selected collocation points	Scale-3 HW solution	Exact solution
$(\frac{40.5}{81}, \frac{40.5}{81})$	-0.0609408	-0.060941
$(\frac{8.5}{81}, \frac{8.5}{81})$	-0.00829978	-0.00829971
$(\frac{24.5}{81}, \frac{8.5}{81})$	-0.0208576	-0.0208574
$(\frac{76.5}{81}, \frac{6.5}{81})$	-0.00354928	-0.00354924
$(\frac{1.5}{81}, \frac{79.5}{81})$	-0.00030456	-0.00030455
$(\frac{45.5}{81}, \frac{77.5}{81})$	-0.0114989	-0.0114988
$(\frac{65.5}{81}, \frac{58.5}{81})$	-0.0286731	-0.0286731
$(\frac{14.5}{81}, \frac{55.5}{81})$	-0.0287463	-0.0287463
$(\frac{27.5}{81}, \frac{32.5}{81})$	-0.0516417	-0.0516418
$(\frac{58.5}{81}, \frac{41.5}{81})$	-0.0466601	-0.0466602

D. Problem 4:

Consider the steady state heat distribution in a unit plane where two sides are insulated, which leads to a set of both Dirichlet and Neumann boundary conditions.

$$\frac{\partial^2 u}{\partial x^2} + \frac{\partial^2 u}{\partial y^2} = -8\pi^2 sin(2\pi x) sin(2\pi y) \tag{48}$$

Boundary conditions are

$$u_x(0, y) = 2\pi sin(2\pi y)$$
$$u_x(1, y) = 2\pi sin(2\pi y)$$
$$u(x, 0) = 0$$
$$u(x, 1) = 0$$

Exact solution for this problem is

$$u(x, y) = sin(2\pi x) sin(2\pi y). \tag{49}$$

The approximation is carried out as said in Section 5, and we get,

$$u(x) = \sum_{i=1}^{3M} c_i p_{2,i}(x) + \frac{\partial u(0)}{\partial x}(x) + u(0) \tag{50}$$

$$\frac{\partial u(x)}{\partial x} = \sum_{i=1}^{3M} c_i p_{1,i}(x) + \frac{\partial u(0)}{\partial x} \tag{51}$$

along x direction and

$$\frac{\partial u(y)}{\partial y} = \sum_{i=1}^{3M} c_i p_{1,i}(y) + \frac{\partial u(0)}{\partial y} \tag{52}$$

$$u(y) = \sum_{i=1}^{3M} c_i p_{2,i}(y) + \frac{\partial u(0)}{\partial y}(y) + u(0) \tag{53}$$

along y direction respectively. Using given Dirichlet and Neumann boundary conditions, the additional equations can be written as

$$f_{ex1} = \begin{bmatrix} p_{1,1}(0) & p_{1,2}(0) & \cdots & p_{1,3M}(0) & 1 & 0 \\ p_{1,1}(1) & p_{1,2}(1) & \cdots & p_{1,3M}(1) & 1 & 0 \end{bmatrix} \begin{bmatrix} c \\ b_1 \end{bmatrix} \tag{54}$$

$$f_{ex2} = \begin{bmatrix} p_{2,1}(0) & p_{2,2}(0) & \cdots & p_{2,3M}(0) & 0 & 1 \\ p_{2,1}(1) & p_{2,2}(1) & \cdots & p_{2,3M}(1) & 1 & 1 \end{bmatrix} \begin{bmatrix} d \\ b_2 \end{bmatrix} \tag{55}$$

where $b_1^T = (\frac{\partial u(0)}{\partial x}, u(0))$, $b_2^T = (\frac{\partial u(0)}{\partial y}, u(0))$ and $c^T = (c_1, c_2, \ldots, c_{3M})$, $d^T = (d_1, d_2, \ldots, d_{3M})$ are Haar coefficients along x and y directions respectively. After extending the approximation to the $2D$ domain we get,

$$\frac{\partial^2 \mathbf{u}(\mathbf{x_l}, \mathbf{y_k})}{\partial \mathbf{x^2}} = (\mathbf{B_1} \otimes \mathbf{I_y})\mathbf{u}(\mathbf{x_l}, \mathbf{y_k}) + (\mathbf{B_2} \otimes \mathbf{I_y})\mathbf{f_1}$$
$$= \mathbf{D_x}\mathbf{u}(\mathbf{x_l}, \mathbf{y_k}) + \mathbf{k_x}$$

$$\frac{\partial^2 \mathbf{u}(\mathbf{x_l}, \mathbf{y_k})}{\partial \mathbf{y^2}} = (\mathbf{I_x} \otimes \mathbf{B_3})\mathbf{u}(\mathbf{x_l}, \mathbf{y_k}) + (\mathbf{I_x} \otimes \mathbf{B_4})\mathbf{f_2}$$
$$= \mathbf{D_y}\mathbf{u}(\mathbf{x_l}, \mathbf{y_k}) + \mathbf{k_y}$$

Here $\mathbf{f_1}$ and $\mathbf{f_2}$ are $6M \times 1$ column vectors where $\mathbf{f_1}^T = (2\pi sin(2\pi x_1), \ldots, 2\pi sin(2\pi x_{3M}), 2\pi sin(2\pi x_1), \ldots,$

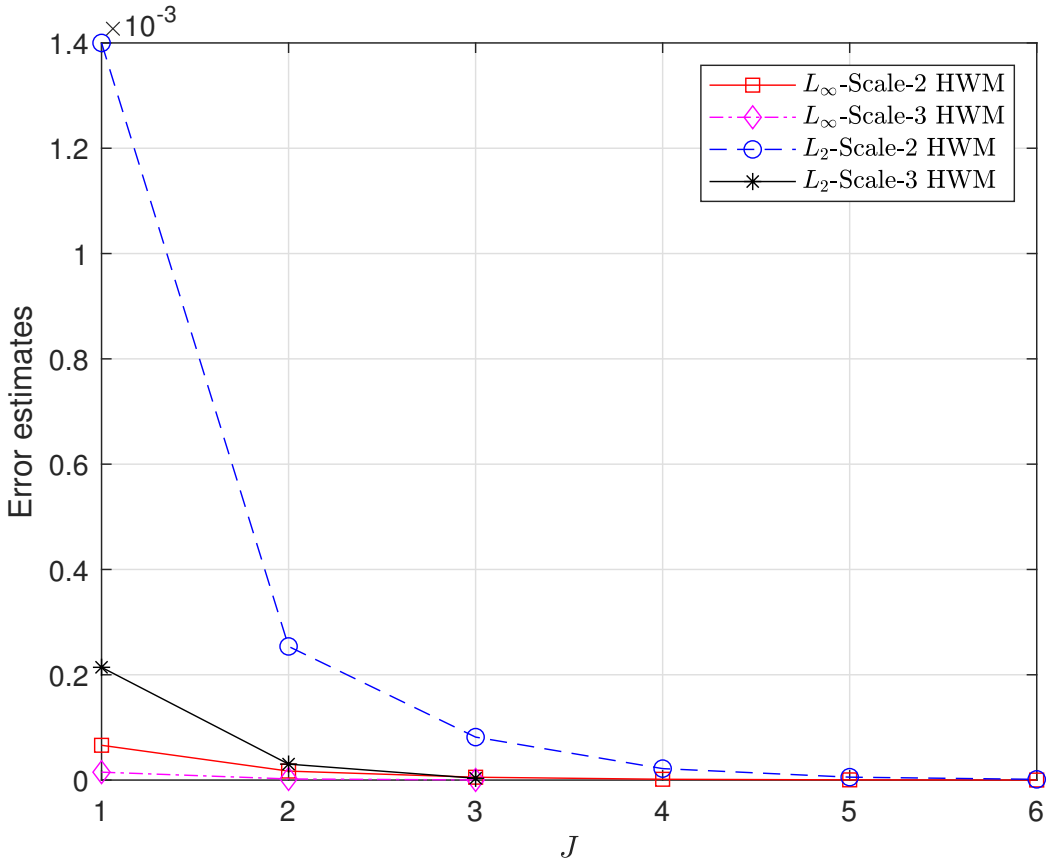

Fig. 12: Error estimates at different resolution levels for Problem 3.

TABLE VIII: Evaluation of the numerical accuracy of Scale-3 HWM and FDM solutions for Problem 3.

Points	L_∞		L_2	
	FDM	Scale-3 HW	FDM	Scale-3 HW
9	4.7044E-05	1.5041E-05	6.8154E-04	2.1417E-04
27	4.8105E-06	2.1550E-06	6.7221E-05	3.0329E-05
81	5.1095E-07	2.4871E-07	7.1208E-06	3.4625E-06

TABLE IX: Comparison of Scale-3 HWM with Scale-2 HWM and FDM for Problem 4.

J	Scale-2 HW			FDM			Scale-3 HW			Order of convergence (O_c)	
	No. of Points	L_2	L_∞	No. of Points	L_2	L_∞	No. of Points	L_2	L_∞	Scale-2 HW	Scale-3 HW
1	4	0.0452	0.0319	9	0.0528	0.0495	9	0.0153	0.0154	-	-
2	8	0.0189	0.0175	27	0.0043	0.0048	27	0.0018	0.0018	0.8662	1.9539
3	16	0.0051	0.0051	81	4.3062E-04	5.1191E-04	81	2.0584E-04	2.3058E-04	1.7788	1.8705
4	32	0.0013	0.0013	-	-	-	-	-	-	1.9720	-
5	64	3.2951E-04	3.6099E-04	-	-	-	-	-	-	1.8485	-
6	128	8.2479E-05	9.5115E-05	-	-	-	-	-	-	1.9242	-

$2\pi sin(2\pi x_{3M}))$ and $\mathbf{f_2} = 0$. Addition of above two equations leads to the following system of equations

$$(\mathbf{D_x}+\mathbf{D_y})\mathbf{u} = -8\pi^2 sin(2\pi \mathbf{x_l}) sin(2\pi \mathbf{y_k}) - \mathbf{k_x} - \mathbf{k_y} \quad (56)$$

The system is solved, and the resulting L_2 error and maximum absolute errors are presented in Table IX, where they are compared with the results of the Scale-2 HW method and the FDM. The CPU time required for computation is recorded for all three methods at various resolution levels and compared in Table X. The results indicate that the Scale-3 HW method surpasses the Scale-2 HW and FDM in terms of accuracy and computational efficiency. A comparison between the numerical solution obtained using above proposed method and the exact solutions at selected ponits is provided in Table XI. Additionally, the numerical solutions and absolute errors are pictorially represented in Figures 14a, 14b and 15, respectively. The color variation

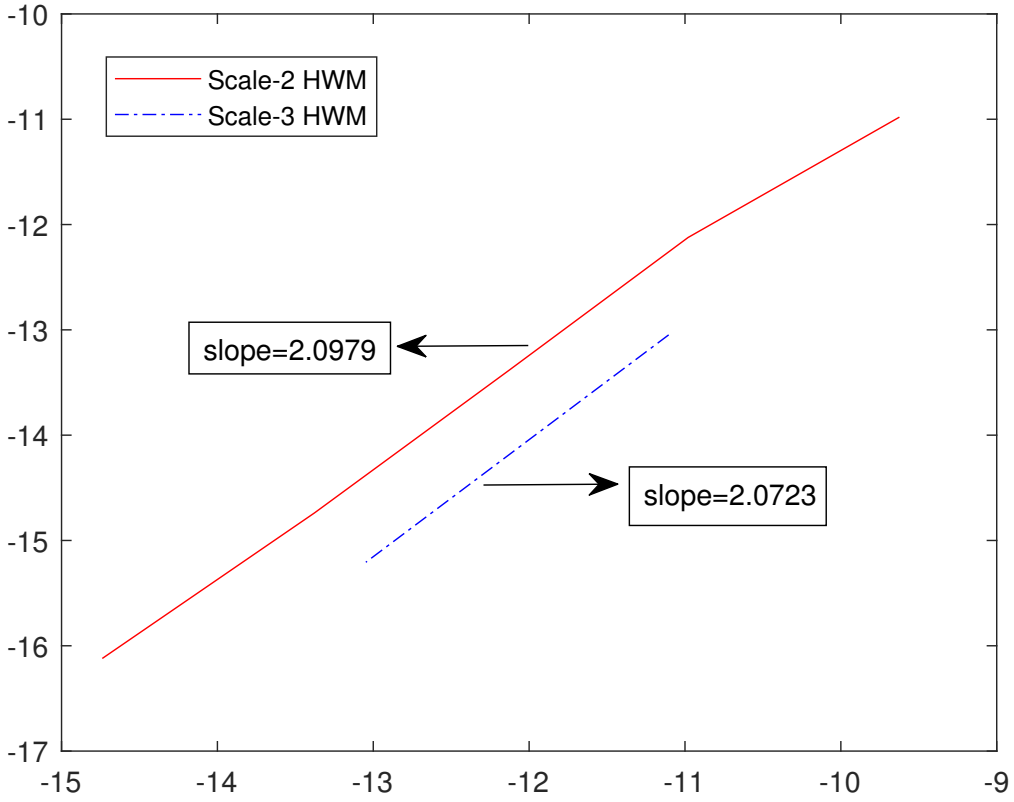

Fig. 13: Numerical order of convergence for Problem 3 using $log - log$ plot.

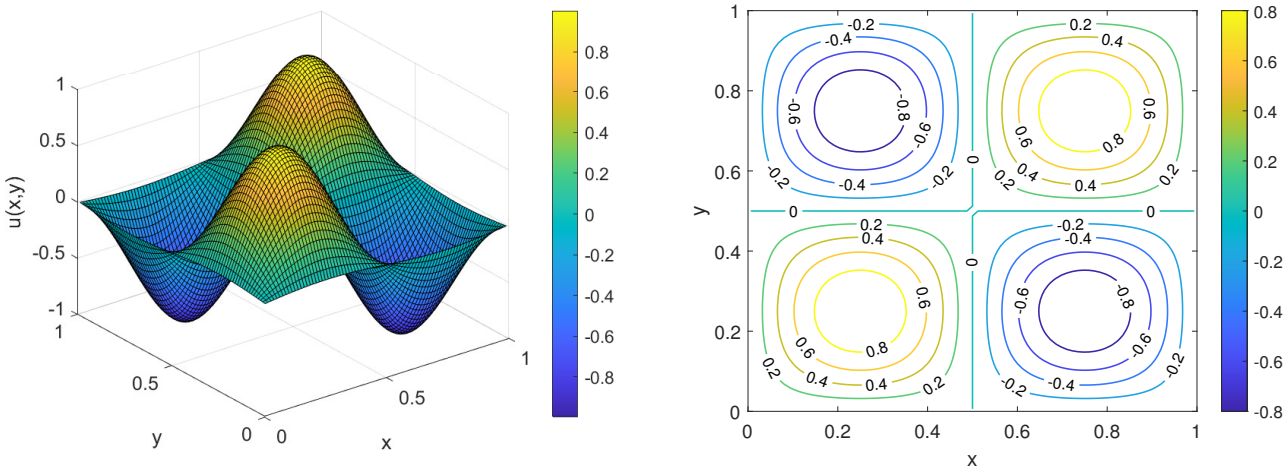

(a) Surface plot.

(b) Contour plot.

Fig. 14: Scale-3 HW solution plot at resolution level $J = 3$ for Problem 4.

in Figure 15 illustrate the error distribution across different points, with lighter shades indicating higher errors and darker shades representing lower errors. The choice of boundary condition significantly impacts the error distribution in Figures 15 and 16. Specifically, the Neumann conditions at the left and right boundaries result in higher errors than the Dirichlet conditions applied to the top and bottom boundaries.

VII. Conclusion

In this study, three different numerical methods, the Scale-3 HW method, the Scale-2 HW method, and the Finite Difference Method were compared for solving the steady-state heat distribution equation in terms of error estimates and computational efficiency. The results demonstrate that the Scale-3 HW method outperforms both the Scale-2 HW method and FDM, achieving higher accuracy with lower L_2 and L_∞ errors. Additionally,

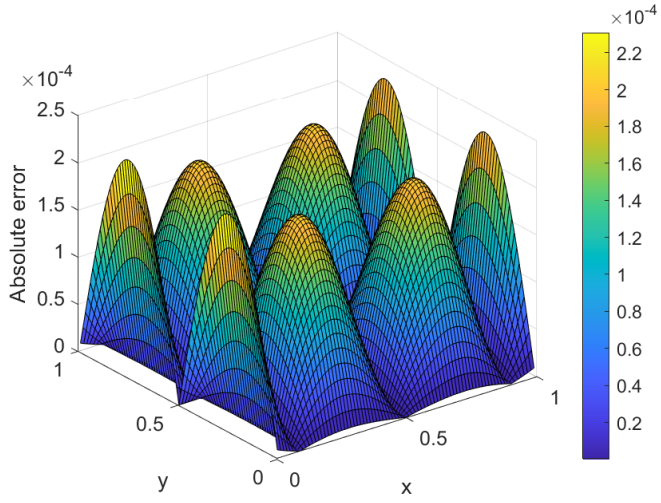

Fig. 15: Absolute error plot at resolution level $J = 3$ for Problem 4.

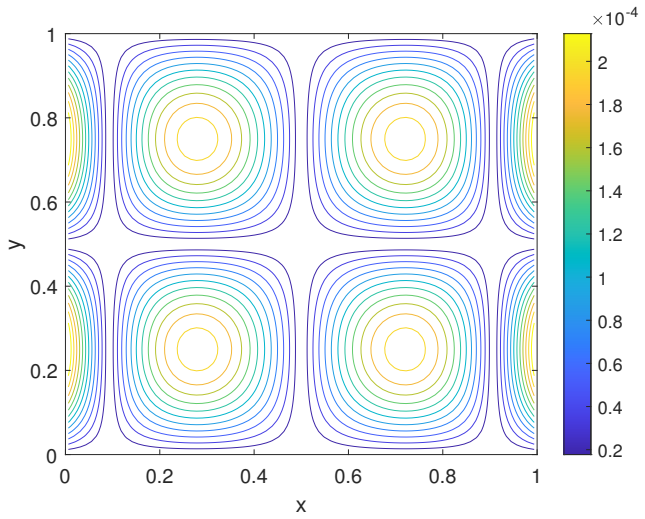

Fig. 16: Contour plot of absolute error at resolution level $J = 3$ for Problem 4.

TABLE X: Time comparison in Problem 4.

J	Scale-2 HW		FDM		Scale-3 HW	
	No. of Points	CPU Time (s)	No. of Points	CPU Time (s)	No. of Points	CPU Time (s)
1	4	0.0156	9	0.0469	9	0.0156
2	8	0.0156	27	0.0938	27	0.0625
3	16	0.0312	81	6.6406	81	4.6094
4	32	0.1562	-	-	-	-
5	64	1.6875	-	-	-	-
6	128	63.578	-	-	-	-

the computational time required for the Scale-3 HW method is significantly reduced compared to the other two approaches, highlighting its efficiency in handling high-resolution solutions. The superior performance of the Scale-3 HW method can be attributed to its better approximation properties and adaptability to complex functions, making it a good choice for solving PDEs. The comparison of numerical and exact solutions at selected points further confirms its accuracy. The error distribution

TABLE XI: Numerical and exact solution at some collocation points for Problem 4 at $J = 3$.

Selected collocation points	Scale-3 HW solution	Exact solution
$\left(\frac{40.5}{81}, \frac{40.5}{81}\right)$	9.30483e-15	0
$\left(\frac{8.5}{81}, \frac{8.5}{81}\right)$	0.375264	0.375279
$\left(\frac{24.5}{81}, \frac{8.5}{81}\right)$	0.579487	0.579611
$\left(\frac{76.5}{81}, \frac{6.5}{81}\right)$	-0.165278	-0.165234
$\left(\frac{1.5}{81}, \frac{79.5}{81}\right)$	-0.0135	-0.013478
$\left(\frac{45.5}{81}, \frac{77.5}{81}\right)$	0.1014	0.101423
$\left(\frac{65.5}{81}, \frac{58.5}{81}\right)$	0.918553	0.918711
$\left(\frac{14.5}{81}, \frac{55.5}{81}\right)$	-0.82825	-0.828385
$\left(\frac{27.5}{81}, \frac{32.5}{81}\right)$	0.491826	0.491934
$\left(\frac{58.5}{81}, \frac{41.5}{81}\right)$	0.0762992	0.0763151

visualization also reveals that the Scale-3 HW method minimizes local errors more effectively than the Scale-2 HW and FDM methods. Future work may involve extending the method to higher-dimensional PDEs and nonlinear problems and applying the method to real-world applications in engineering, physics, and finance to validate its practical effectiveness using quantum computing techniques.

ACKNOWLEDGMENT

The authors thank Manipal Academy of Higher Education for the constant encouragement to conduct research work.

REFERENCES

[1] B. E. Gatewood, "XXIII. thermal stresses in long cylindrical bodies," *The London, Edinburgh, and Dublin Philosophical Magazine and Journal of Science*, vol. 32, no. 213, pp. 282–301, 1941.

[2] M. N. Akhtar, M. H. Durad, A. Usman *et al.*, "Steady state heat transfer using Galerkin finite element method," in *2015 Fourth International Conference on Aerospace Science and Engineering (ICASE)*. IEEE, 2015, pp. 1–6.

[3] T. Conroy, M. N. Collins, and R. Grimes, "A review of steady-state thermal and mechanical modelling on tubular solar receivers," *Renewable and Sustainable Energy Reviews*, vol. 119, p. 109591, 2020.

[4] A. Boutayeb and E. Twizell, "Finite-difference methods for the solution of special eighth-order boundary-value problems," *International Journal of Computer Mathematics*, vol. 48, no. 1-2, pp. 63–75, 1993.

[5] L. Gavete, F. Ureña, J. J. Benito, A. García, M. Ureña, and E. Salete, "Solving second order non-linear elliptic partial differential equations using generalized finite difference method," *Journal of Computational and Applied Mathematics*, vol. 318, pp. 378–387, 2017.

[6] P. Ŝolín, *Partial Differential Equations and the Finite Element Method*. Hoboken, New Jersey: John Wiley & Sons, 2005.

[7] E. Caburnay and L. D. E. Magdaluyo Jr, "Finite Element Analysis of an External Fixator with Composite Connecting Rods," *Proceedings of the International MultiConference of Engineers and Computer Scientists 2023*, vol. 2243, 2023.

[8] S. Mazumder, *Numerical Methods for Partial Differential Equations: Finite Difference and Finite Volume Methods*. 125 London Wall, EC2Y 5AS, UK: Academic Press, 2015.

[9] S. M. Guzik, X. Gao, and C. Olschanowsky, "A high-performance finite-volume algorithm for solving partial differential equations governing compressible viscous flows on structured grids," *Computers & Mathematics with Applications*, vol. 72, no. 9, pp. 2098–2118, 2016.

[10] X.-W. Gao, Y.-M. Zhu, and T. Pan, "Finite line method for solving high-order partial differential equations in science and engineering," *Partial Differential Equations in Applied Mathematics*, vol. 7, p. 100477, 2023.

[11] H. Khan, R. Shah, P. Kumam, and M. Arif, "Analytical Solutions of Fractional-Order Heat and Wave Equations by the Natural Transform Decomposition Method," *Entropy*, vol. 21, no. 6, p. 597, 2019.
[12] N. Kumar and R. K. Dubey, "A new development of sixth order accurate compact scheme for the Helmholtz equation," *Journal of Applied Mathematics and Computing*, vol. 62, no. 1, pp. 637–662, 2020.
[13] H. Ren, X. Zhuang, and T. Rabczuk, "A nonlocal operator method for solving partial differential equations," *Computer Methods in Applied Mechanics and Engineering*, vol. 358, p. 112621, 2020.
[14] T. C. Mahor, R. Mishra, and R. Jain, "Analytical solutions of linear fractional partial differential equations using fractional Fourier transform," *Journal of Computational and Applied Mathematics*, vol. 385, p. 113202, 2021.
[15] C. Uriarte, D. Pardo, and Á. J. Omella, "A Finite Element based Deep Learning solver for parametric PDEs," *Computer Methods in Applied Mechanics and Engineering*, vol. 391, p. 114562, 2022.
[16] Z. Zheng, M. Valdebenito, M. Beer, and U. Nackenhorst, "A stochastic finite element scheme for solving partial differential equations defined on random domains," *Computer Methods in Applied Mechanics and Engineering*, vol. 405, p. 115860, 2023.
[17] R. Saadeh, L. Hamdi, and A. Qazza, "Double Laplace Formable Transform Method for Solving PDEs," *Engineering Letters*, vol. 32, no. 3, pp. 579–587, 2024.
[18] M. I. Azis, "A Combined Laplace Transform and Boundary Element Method for Unsteady Modified Helmholtz Type Problems of Anisotropic Quadratically Graded Materials," *Proceedings of the World Congress on Engineering 2021*, vol. 2242, 2021.
[19] J. Delgado, "Analytical Study of a Semilinear Problem With Dirichlet Boundary Conditions," *IAENG International Journal of Applied Mathematics*, vol. 54, no. 12, pp. 2580–2587, 2024.
[20] S. Elbostani and R. El Jid, "A Meshless Method Based on the Moving Least Squares Approach for Approximate Solution of the Generalized 2-D Nonlinear Benjamin–Bona–Mahony–Burgers Equation," *IAENG International Journal of Applied Mathematics*, vol. 54, no. 9, pp. 1734–1746, 2024.
[21] H. Karkera, S. K. Shettigar, and N. N. Katagi, "A Comparative Study of Two Wavelet-Based Numerical Schemes for the Solution of Nonlinear Boundary Value Problems," *IAENG International Journal of Applied Mathematics*, vol. 54, no. 9, pp. 1894–1904, 2024.
[22] H. Karkera, N. N. Katagi, and R. B. Kudenatti, "Analysis of general unified MHD boundary-layer flow of a viscous fluid-a novel numerical approach through wavelets," *Mathematics and Computers in Simulation*, vol. 168, pp. 135–154, 2020.
[23] I. Daubechies, "Ten Lectures on Wavelets," *Society for industrial and applied mathematics*, 1992.
[24] J. Mouley, N. Sarkar, and S. De, "A study of Griffith crack in nonlocal infinite magneto-elastic media," *International Journal for Computational Methods in Engineering Science and Mechanics*, vol. 25, no. 4, pp. 177–192, 2024.
[25] B. Hussain, M. Faheem, and A. Khan, "A numerical technique based on Legendre wavelet for linear and nonlinear hyperbolic telegraph equation," *Journal of Applied Mathematics and Computing*, pp. 1–24, 2024.
[26] A. Haar, "On the Theory of Orthogonal Function Systems," *Mathematische Annalen*, vol. 69, no. 3, pp. 331–371, 1910.
[27] C. Cattani, "Haar Wavelet Splines," *Journal of Interdisciplinary Mathematics*, vol. 4, no. 1, pp. 35–47, 2001.
[28] C. F. Chen and C.-H. Hsiao, "Haar wavelet method for solving lumped and distributed-parameter systems," *IEE Proceedings-Control Theory and Applications*, vol. 144, no. 1, pp. 87–94, 1997.
[29] C.-H. Hsiao, "State analysis of linear time delayed systems via Haar wavelets," *Mathematics and Computers in Simulation*, vol. 44, no. 5, pp. 457–470, 1997.
[30] Ü. Lepik, "Numerical solution of differential equations using Haar wavelets," *Mathematics and computers in simulation*, vol. 68, no. 2, pp. 127–143, 2005.
[31] ——, "Numerical solution of evolution equations by the Haar wavelet method," *Applied Mathematics and Computation*, vol. 185, no. 1, pp. 695–704, 2007.
[32] ——, "Solving PDEs with the aid of two-dimensional Haar wavelets," *Computers & Mathematics with Applications*, vol. 61, no. 7, pp. 1873–1879, 2011.
[33] Z. Shi, Y.-y. Cao, and Q.-j. Chen, "Solving 2D and 3D Poisson equations and biharmonic equations by the Haar wavelet method," *Applied Mathematical Modelling*, vol. 36, no. 11, pp. 5143–5161, 2012.
[34] S. Zhi, X. Yan-Hua, and Z. Jun-Ping, "Haar wavelets method for solving Poisson equations with jump conditions in irregular domain," *Advances in Computational Mathematics*, vol. 42, pp. 995–1012, 2016.
[35] G. Hariharan and K. Kannan, "A Comparative Study of a Haar Wavelet Method and a Restrictive Taylor's Series Method for Solving Convection-diffusion Equations," *International Journal for Computational Methods in Engineering Science and Mechanics*, vol. 11, no. 4, pp. 173–184, 2010.
[36] R. Mittal and S. Pandit, "Quasilinearized Scale-3 Haar wavelets-based algorithm for numerical simulation of fractional dynamical systems," *Engineering Computations*, vol. 35, no. 5, pp. 1907–1931, 2018.
[37] ——, "New Scale-3 Haar Wavelets Algorithm for Numerical Simulation of Second Order Ordinary Differential Equations," *Proceedings of the National Academy of Sciences, India Section A: Physical Sciences*, vol. 89, pp. 799–808, 2019.
[38] S. Pandit and R. Mittal, "A numerical algorithm based on Scale-3 Haar wavelets for fractional advection dispersion equation," *Engineering Computations*, vol. 38, no. 4, pp. 1706–1724, 2021.
[39] R. Kumar and S. Bakhtawar, "An Improved Algorithm based on Haar Scale 3 Wavelets for the Numerical Solution of Integro-differential Equations," *Mathematics in Engineering, Science & Aerospace (MESA)*, vol. 13, no. 2, pp. 617–633, 2022.